Journal of Energy Storage 50 (2022) 104570

Contents lists available at ScienceDirect

Journal of Energy Storage

journal homepage: www.elsevier.com/locate/est

Power-to-heat integration in regenerator storage: Enhancing thermal storage capacity and performance

Sergej Belik *, Volker Dreissigacker, Stefan Zunft

Institute of Engineering Thermodynamics, German Aerospace Center (DLR), Stuttgart, Germany

ARTICLE INFO

Keywords:
Power-to-heat
Electric flow heater
Regenerator storage
Electrothermal energy storage
Storage power plant
Thermodynamic analysis

ABSTRACT

Electrically heated regenerator storage is an energy- and cost-efficient solution for converting excess electricity and storing it as high-temperature heat. We introduce a transient model to describe the thermodynamic behavior of this hybrid storage system with the fewest number of dimensionless parameters. These characteristic parameters are used to derive key performance indicators for the thermodynamic assessment of the power-to-heat integration in regenerator storage. The results obtained from simulation studies indicate the energy-efficient location of electric heating elements inside the storage tank and provide designs with significantly improved thermal storage capacity and performance. These benefits from power-to-heat extension are particularly evident in the increased cost efficiency and operational flexibility.

1. Introduction

Electrically heated regenerator storage has recently received significant attention for applications in storage power plants [1,2], electrothermal energy storage [3] and Brayton based pumped thermal electricity storage [4] due to the feasibility of converting excess electricity into heat and storing it cost effectively at various temperature levels [5]. This heat is then reconverted by a power cycle to produce electricity on demand [6,7]. As illustrated in Fig. 1, such a storage system connects a power unit, which is an electric flow heater (EFH), with a solid media thermal energy storage (STES) unit.

1.1. Power-to-heat unit: electric flow heater

High temperature EFHs are currently used industrially in various types and power levels [8,9]. In the megawatt scale, the most common type is the tubular EFH [9]. This type offers a large heat transfer area and is primarily used in plant engineering as well as in the chemical industry for drying and air-conditioning with gaseous media [10]. The gaseous heat transfer fluid (HTF), which is typically air, flows in direct contact along the tubular heating elements, providing high-temperature process heat at maximum gas temperatures in the range of 600 to 700 °C [9]. This power-to-heat technology provides high-temperature heat at low costs and is proposed by many authors to charge the STES unit in various storage applications [3–5].

1.2. Storage unit: solid media thermal energy storage

The STES is a counterflow regenerator thermal energy storage (TES) unit that has been proven in high-temperature applications for the steelmaking and glass industries [11]. The basic concept consists of a thermally insulated reservoir through which hot gas flows, transferring heat to the porous solid media in direct contact. After this charging period, the source of gas changes from hot to cold so that the stored thermal energy is recovered by the cold gas. A gaseous HTF, such as air, is used in combination with high-temperature inventory materials, including perforated bricks, rocks, slag and ceramics. For such low-cost materials, the maximum operating temperature ranges from 800 to 1200 °C [5,7,11].

Numerous theoretical research studies have addressed the modeling and thermodynamic analysis of the regenerator storage. In addition to the extensive work by Hausen [12] and Schumann [13], Schmidt and Willmott [14] provide a comprehensive collection of several modeling approaches and derived design techniques based on First Law considerations. Both contributions serve as a basis for various theoretical [11,15,16] and experimental works [11,17,18] that further investigate the STES unit. In addition to the mentioned contributions, Singh et al. [19] and Escene et al. [20] perform a comprehensive literature study on numerous publications investigating the conception, thermodynamic behavior and design of the STES component.

* Corresponding author.
E-mail address: Sergej.Belik@dlr.de (S. Belik).

https://doi.org/10.1016/j.est.2022.104570
Received 10 September 2021; Received in revised form 23 March 2022; Accepted 29 March 2022
Available online 19 April 2022

Nomenclature

a_v	surface area to volume ratio related to the solid phase (m^{-1})
a_w	surface area to volume ratio related to the wall (m^{-1})
c_p	specific heat capacity (J kg^{-1} K^{-1})
C_{TES}	ratio of STES storage capacity to the amount of energy delivered by STES
f_{mat}	material related factor, see Eqs. (8a) and (8b)
H	total length (m)
k_v	heat transfer coefficient related to the solid phase (W m^{-2} K^{-1})
m	storage mass (kg)
$\dot{m}_f$	mass flow rate (kg s^{-1})
P_{el}	electrical power input (W)
$\dot{Q}_{PtH}$	Joule heat induced by electric heating (W)
$\dot{q}_{PtH}$	Joule heat power density (W m^{-3})
$q_{EH-STES}^*$	averaged gravimetric energy density (J kg^{-1} K^{-1}), see Eq. (16)
St	Stanton number
t	time scale (s)
$\Delta T_{f,drop}$	relative outlet temperature drop during discharging (%)
$T_{f,in}$	normalized inlet temperature (−)
$\overline{T}'_{f,out}$	normalized averaged outlet temperature
$T'_{f,out,mix}$	normalized temperature at the mixing point for bypass operation
U_w	heat transfer coefficient related to the wall (W m^{-2} K^{-1})
V	volume (m^3)
w_f	free flow velocity (m s^{-1})
z	length scale (m)
z_{EFH}	dimensionless heating area, H_{EFH}/H

Greek symbols

ε	void fraction (−)
ζ	storage utilization ratio, see Eqs. (17a) and (17b)
η_{PtH}	electric heating efficiency, $\dot{Q}_{PtH}/P_{el}$
η_{ex}	exergetic efficiency
ϑ	temperature (K)
$\Delta\vartheta_{in}$	maximum inlet temperature difference between charging and discharging (K)
λ	thermal conductivity (W m^{-1} K^{-1})
ξ	coefficient of uniformity, see Eq. (19)
ρ	density (kg m^{-3})
τ	duration of charging period (s)
Γ	dimensionless loss number
Λ	reduced (dimensionless) length
Π	reduced (dimensionless) period duration
Φ	dimensionless heat source number
$\dot{X}_{EFH}$	dimensionless exergy rate, see Eq. (12)

Subscripts

EH-STE	electrically heated STES
EFH	electric flow heater
HTF	heat transfer fluid
PtH	power-to-heat
STES	solid media thermal energy storage
TES	thermal energy storage
in	inlet
out	outlet
s	solid phase
f	fluid phase (heat transfer fluid)
0	ambient

Superscripts

′	related to discharging period
$\overline{x}$	averaged quantity x
x^*	normalized quantity x

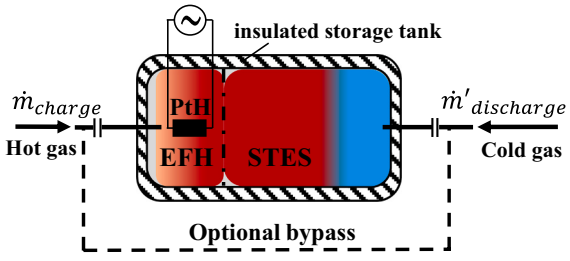

Fig. 1. Schematic representation of a solid media thermal energy storage system with an electric flow heater and optional discharging bypass.

1.3. Electrically heated solid media thermal energy storage: Scope and method

The object of our detailed investigation is a storage system referred to as an electrically heated STES (EH-STES) system. According to Fig. 1, this hybrid system comprises an EFH component connected to a STES component. The EFH is located either inside the thermal reservoir, as indicated in the Fig. 1 scheme, or outside. A gaseous HTF transports high-temperature heat from the EFH to the STES unit during the charging operation. The discharge principle is similar to that of the counterflow regenerator, except that the sensible heat of the EFH is used in addition to the recovered heat of the STES.

Few existing scientific publications have investigated EH-STES systems. Forsberg et al. [7] and Stack et al. [5] propose a concept referred to as FIRES, which consists of metallic heater wires contacted with a firebrick storage medium to heat it to temperatures above 1000 °C. During this charging process, the heater wires transfer the heat to the storage material via thermal radiation and thermal conduction. The discharging process is analogous to the regenerator storage. This investigation focuses on the discharging process using a one-dimensional approach to model the thermal energy storage. The heat source term is simply formulated by a constant heat flux boundary condition [7]. Zubair et al. [21] analyze a similar concept, focusing on the thermoeconomics of the storage system. The power-to-heat (PtH) source term is given by a constant electric power without detailed modeling of the heating component. Furthermore, Dreissigacker et al. [22] and Houssainy et al. [23] propose a storage system consisting of an EFH connected in series with a packed bed TES unit. This STES component is described by a simplified transient and one-dimensional model considering the thermal resistance within the packed bed. The EFH component, in contrast, is modeled by a stationary model that assumes an ideal conversion of electric to thermal power.

The presented literature survey shows that investigations of EH-STES systems have focused on detailed modeling of the STES unit. The electric heater, conversely, has been modeled in a simplified way based on stationary models so that statements about component size and transient heat transfer behavior in combination with a STES unit cannot be conducted. Therefore, the purpose of the present contribution is to introduce and apply a numerical model that describes the thermodynamic

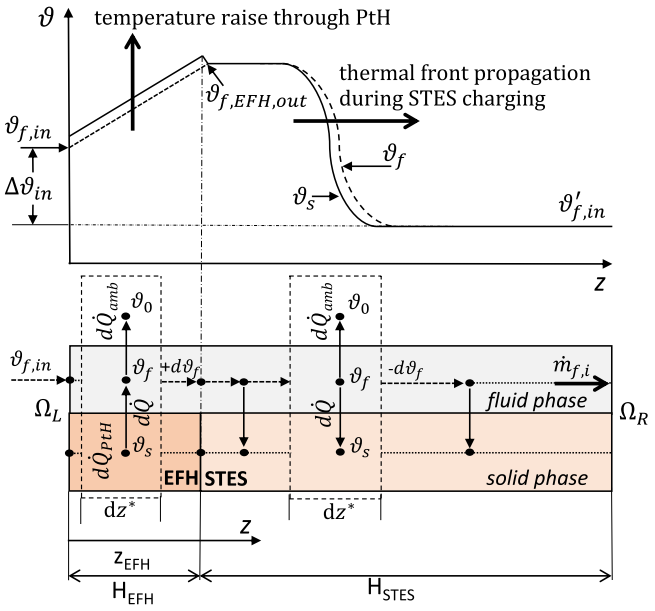

Fig. 2. Schematic illustration of temperature profiles during charging mode with associated discretization scheme of the two-phase region.

behavior of both components in one hybrid storage system.

To this end, we propose a compact and dimensionless model that describes the thermodynamic behavior of the EH-STES system with the fewest number of characteristic parameters. The first step is to simplify the one-dimensional model provided by Schumann [13] and develop it into a formulation with dimensionless parameters. These characteristic parameters are used in a second step to derive technical key performance indicators (KPIs) for assessing the PtH integration. Subsequently, a simulation study is conducted varying characteristic parameters to identify the most beneficial location for the electric heating elements in terms of energy density and corresponding thermodynamic efficiency. Another simulation study shows the impact of PtH integration on the thermal storage capacity and provides recommendations for energy-efficient design solutions with maximum storage utilization. The final study quantifies the improvement in storage performance based on power-related KPIs.

2. Model description

The objective of the numerical analysis is to develop the simplest possible but nontrivial model that enables the calculation of the thermodynamic behavior of the EFH and STES unit under cyclic conditions. Consequently, Schumann's simplified two-phase transient and one-dimensional model [13,16] is used as a basis for further modifications. This modeling approach only considers heat transport in the axial direction. It neglects heat conduction in this direction due to the low effective thermal conductivity for both the solid and fluid phases. Moreover, no heat generation is considered in this model.

In addition to these assumptions, the following simplifications are made:

- the accumulation term of the fluid phase is neglected due to its marginal thermal capacity.
- the solid and fluid thermophysical properties are temperature independent.
- the influence of the thermal resistance inside the solid media is neglected since the heat transfer resistance dominates with a small biot number (Bi <0.10).

As depicted in Fig. 2, modifications to this model include separating the solid phase into two regions, one for the TES inventory and another for the EFH heating area and its occurring heat generation. This heat is produced according to the principle of Joule heating and is considered with a source term in Eq. (1b), which is the heat balance equation of the solid phase. In the fluid phase, the term for thermal losses to the ambient is considered for both components. With these considerations, the temporally and spatially varying temperature field during thermal cyclic operation is calculated for both phases as well as for both components, the STES unit (Eq. notation 'a') and the EFH unit (Eq. notation 'b').

Solid phase of the STES unit:

$$\frac{d\vartheta_s}{dt} = \frac{k_v\, a_v}{(1-\varepsilon)\rho_{TES} c_{p,TES}} \left(\vartheta_f - \vartheta_s\right) \tag{1a}$$

with adiabatic boundary condition at $\Omega_R: -\lambda \frac{\partial \vartheta_{TES}}{\partial z} = 0$

Solid phase of the EFH unit:

$$\frac{d\vartheta_s}{dt} = \frac{\dot{Q}_{PtH}}{V_{EFH}(1-\varepsilon)\rho_{EFH} c_{p,EFH}} + \frac{k_v\, a_v}{(1-\varepsilon)\rho_{EFH} c_{p,EFH}} \left(\vartheta_f - \vartheta_s\right) \tag{1b}$$

with adiabatic boundary condition at $\Omega_L: -\lambda \frac{\partial \vartheta_{EFH}}{\partial z} = 0$

Fluid phase of the STES unit:

$$\frac{d\vartheta_f}{dz_{TES}} = \frac{k_v\, a_v}{w_f\, \varepsilon\, \rho_f\, c_{p,f}} \left(\vartheta_s - \vartheta_f\right) - \frac{U_w\, a_w}{w_f\, \varepsilon\, \rho_f\, c_{p,f}} \left(\vartheta_f - \vartheta_0\right) \tag{2a}$$

with adiabatic boundary condition at $\Omega_R: -\lambda \frac{\partial \vartheta_f}{\partial z} = 0$

Fluid phase of the EFH unit:

$$\frac{d\vartheta_f}{dz_{EFH}} = \frac{k_v\, a_v}{w_f\, \varepsilon\, \rho_f\, c_{p,f}} \left(\vartheta_s - \vartheta_f\right) - \frac{U_w\, a_w}{w_f\, \varepsilon\, \rho_f\, c_{p,f}} \left(\vartheta_f - \vartheta_0\right) \tag{2b}$$

with constant temperature boundary conditions for the inlet at $\Omega_L: T_f = \frac{\vartheta_{f,in}}{\Delta\vartheta_{in}}$ where ϑ_s and ϑ_f represent the solid medium and the HTF temperatures of the EFH and the STES unit for the convective heat transfer. In addition to this heat transfer mechanism, heat losses to the ambient are described on the right-hand side of Eq. (2b) using the reference temperature ϑ_0. Moreover, $\dot{Q}_{PtH}$ represents the electrically produced heat inside the total volume V_{EFH} of the EFH body; k_v and U_w denote the heat transfer coefficients to the porous media and to the wall together with the related surface area to volume ratios a_v and a_w. Furthermore, w_f represents the HTF velocity and ε gives the void fraction. The specific heat capacity c_p and the density ρ are given for the solid and fluid media, respectively. For simplicity, the STES unit and EFH void fractions are assumed to be equal, as well as the surface area to volume ratio a_v.

Assuming a balanced and symmetric operation of the EH-STES system with an identical duration of charging and discharging periods ($\tau = \tau'$); identical mass flow rates ($\dot{m}_f = \dot{m}'_f$) and additional normalization in the time $dt = dt^* * \tau$, space $dz = dz^* * H$ and temperature $d\vartheta_{s,f} = dT_{s,f} * \Delta\vartheta_{in}$, Eqs. (1a), (1b) and Eqs. (2a), (2b) may be expressed in the normalized form with the referenced temperature $\Delta\vartheta_{in}$, which is also the maximum temperature difference between the HTF inlets during charging and discharging: $\Delta\vartheta_{in} = \vartheta_{f,\,in} - \vartheta'_{f,\,in}$.

Solid phase:

$$\frac{dT_{s,TES}}{dt^*} = \frac{St_{TES}}{1-\varepsilon} \frac{\left(\vartheta_{f,TES} - \vartheta_{s,TES}\right)}{\Delta\vartheta_{in}} \tag{3a}$$

$$\frac{dT_{s,EFH}}{dt^*} = \Phi\, St_{EFH} + \frac{St_{EFH}}{1-\varepsilon} \frac{\left(\vartheta_{f,EFH} - \vartheta_{s,EFH}\right)}{\Delta\vartheta_{in}} \tag{3b}$$

Fluid phase:

$$\frac{dT_{f,TES}}{dz^*_{TES}} = \Lambda_{TES} \frac{\left(\vartheta_{s,TES} - \vartheta_{f,TES}\right)}{\Delta\vartheta_{in}} - \Gamma_{TES} \frac{\left(\vartheta_{f,TES} - \vartheta_0\right)}{\Delta\vartheta_{in}} \tag{4a}$$

$$\frac{dT_{f,EFH}}{dz^*_{EFH}} = \Lambda_{EFH} \frac{\left(\vartheta_{s,EFH} - \vartheta_{f,TES}\right)}{\Delta\vartheta_{in}} - \Gamma_{EFH} \frac{\left(\vartheta_{f,EFH} - \vartheta_0\right)}{\Delta\vartheta_{in}} \tag{4b}$$

Eqs. (3a) through (4b) describe the thermodynamic behavior of the EH-STES system, which is characterized by four dimensionless parameters for the solid media TES and EFH materials. These parameters are defined below:

Reduced (dimensionless) length

$$\Lambda_{TES} = \frac{k_v\, a_v}{w_f\, \varepsilon\, \rho_f\, c_{p,f}} H_{TES} \tag{5a}$$

$$\Lambda_{EFH} = \frac{k_v\, a_v}{w_f\, \varepsilon\, \rho_f\, c_{p,f}} H_{EFH} \tag{5b}$$

The total reduced length Λ may be expressed as the sum of the reduced lengths of the individual components:

$$\Lambda = \Lambda_{TES} + \Lambda_{EFH} \tag{6}$$

Dimensionless loss number

$$\Gamma_{TES} = \frac{U_w a_w}{w_f \varepsilon\, \rho_f c_{p,f}} H_{TES} \tag{7a}$$

$$\Gamma_{EFH} = \frac{U_w a_w}{w_f \varepsilon\, \rho_f c_{p,f}} H_{EFH} \tag{7b}$$

The total dimensionless loss number Γ may be defined by $\Gamma = \Gamma_{TES} + \Gamma_{EFH}$ in analogy to the definition of the total reduced length Λ. Since STES for utility-scale applications have a small surface area to volume ratio a_v [12], thermal insulation losses are neglected for further investigation ($\Gamma = 0$).

Stanton number

$$St_{TES} = \frac{k_v\, a_v\, \tau}{\rho_{TES}\, c_{p,TES}} \tag{8a}$$

$$St_{EFH} = \frac{k_v a_v\, \tau}{\rho_{EFH}\, c_{p,EFH}} = St_{TES} * f_{mat} \tag{8b}$$

Since both numbers differ by material properties, their relationship can be described by the material related factor:

$$f_{mat} = \frac{\rho_{TES}\, c_{p,TES}\, (1-\varepsilon)}{\rho_{EFH}\, c_{p,EFH}\, (1-\varepsilon)} \tag{9}$$

The Stanton number *St* could also be expressed by the reduced period duration Π, which is defined as the dimensionless time available for the thermal front to propagate through the thermal reservoir. Hausen [12] first introduced this parameter together with Λ.

$$St = \Pi(1-\varepsilon) \tag{10}$$

Dimensionless heat source number

$$\Phi = \frac{\dot{Q}_{PtH}}{V_{EFH}(1-\varepsilon)\, k_v\, a_v\, \Delta\vartheta_{in}} = \frac{\dot{q}_{PtH}}{k_v\, a_v\, \Delta\vartheta_{in}} \tag{11}$$

The dimensionless heat source number describes the ratio of the external heat source $\dot{Q}_{PtH}$ to the heat transferred to the HTF. Furthermore, Φ may be expressed by the Joule heat power density $\dot{q}_{PtH}$, which is defined as the electrical power P_{el} converted into heat with the efficiency η_{PtH} inside the solid volume $V_{s,EFH} = V_{EFH}\,(1-\varepsilon)$. According to Ohm's law, this value is also given by the current density J and the electrical resistivity $\rho_{el,PtH}$ of the PtH body:

$$\dot{q}_{PtH} = \frac{P_{el}\, \eta_{PtH}}{V_{EFH}\,(1-\varepsilon)} = |J|^2 \rho_{el,PtH} \tag{12}$$

3. Technical key performance indicators

The derived dimensionless technical parameters allow for a compact and universal technology assessment of the EH-STES system. To this end, the characteristic parameters *St*, Λ and Φ are used to derive the key performance indicators (KPIs), which quantify the influence of the PtH integration in terms of system performance and thermal storage capacity.

The capacity-related KPIs used in this study are the gravimetric energy density and the utilization ratio of the storage material. In addition to the technical assessment, both of these indicators serve as a basis for an economic assessment in terms of capital costs. The performance-related KPI is the coefficient of uniformity, which describes the uniformity of the outlet temperature during discharging. This indicator is essential as it directly evaluates the technology-specific drop in discharge power. This performance-related KPI may be used to calculate operational costs to evaluate the economics of the storage operation. The power-related and capacity-related KPIs are introduced in the following subsections together with the thermodynamic efficiency.

3.1. Thermodynamic efficiency of the storage system

The primary loss mechanism influencing the thermodynamic efficiency of solid media-based regenerators is the charging loss at the outlet of the cold end of the storage tank. This parameter depends on the regenerator length Λ, the heat source number Φ, the resulting temperatures at the cold-end outlet and the exergy loss due to irreversible heat transfer between solid and fluid media. Neglecting the heat losses to the ambient with $\Gamma = 0$, the round-trip efficiency of the EH-STES system may be expressed as:

$$\eta_{EH-STES} = \frac{\dot{m}'_f * c_{p,f} * \int_0^{t^*=1} \left(T'_{f,out-} - T'_{f,in}\right) dt^*}{\dot{m}_f * c_{p,f} * \left(\int_0^{t^*=1} \left(T_{f,in-} T'_{f,in}\right) dt^* + \dot{X}_{EFH} * \tau \right)} \tag{13}$$

The fraction from Eq. (13) can be reduced to a dimensionless expression since we assume a cyclic steady state of the STES operation with identical heat capacity rates during charging and discharging. The heat source of the EFH is considered with the dimensionless exergy rate $\dot{X}_{EFH}$, which equals the fluid temperature raise caused by the EFH:

$$\dot{X}_{EFH} = \Lambda_{EFH}\, \Phi\, (1-\varepsilon) = T_{f,EFH,out} - T_{f,in} \tag{14}$$

The conversion from electrical into thermal energy is assumed without electrical or thermal losses ($\Gamma_{EFH} = 0$), resulting in a maximum PtH efficiency $\eta_{PtH} = 1$. In contrast to this energetic analysis, the specification of the exergetic efficiency is of greater interest for an electrically driven device. Therefore, the exergetic efficiency of the EFH is defined on the basis of the reference temperature T_0:

$$\eta_{ex,EFH} = \frac{\dot{X}_{EFH,out} - \dot{X}_{in}}{\dot{X}_{EFH}} = 1 - \frac{T_0 \left(ln\left(\frac{T_{f,EFH,out}}{T_0}\right) - ln\left(\frac{T_{f,in}}{T_0}\right) \right)}{T_{f,EFH,out} - T_{f,in}} \tag{15}$$

3.2. Gravimetric energy density

The gravimetric energy density cannot be expressed solely based on characteristic parameters. Therefore, averaged heat capacity values for both the EFH and conventional STES materials are assumed with $f_{mat} = 0.6$. The gravimetric energy density is calculated by means of inlet and outlet temperatures for the discharging period and subsequently weighted based on the heating area z_{EFH} of the EFH:

$$z_{EFH} = \frac{\Lambda_{EFH}}{\Lambda_{EFH} + \Lambda_{TES}} = \frac{H_{EFH}}{H_{EFH} + H_{TES}} = \frac{H_{EFH}}{H} \tag{16}$$

Based on the previous temperature normalization, the averaged gravimetric energy density $q_{EH-STES}$* is given in J/kgK:

$$q^*_{TES} = \frac{\Pi_{TES}}{\Lambda_{TES}} c_{p,TES} \left(\overline{T}'_{f,STES,out} - T'_{f,in} \right) \tag{17a}$$

$$q^*_{EFH} = \frac{\Pi_{EFH}}{\Lambda_{EFH}} c_{p,EFH} \left(\overline{T}'_{f,EH-STES,out} - \overline{T}'_{f,STES,out} \right) \tag{17b}$$

$$q^*_{EH-STES} = q^*_{TES}(1 - z_{EFH}) + q^*_{EFH}\, z_{EFH} \tag{18}$$

where $\overline{T}'_{f,STES,out}$ and $\overline{T}'_{f,EH-STES,out}$ are the averaged outlet temperatures of the STES unit and of the EH-STES system.

3.3. Storage utilization ratio

The propagation of the thermal front in the axial direction depends on the Stanton number and on the reduced regenerator length as well as the heat source number. The resulting temperature profile of the solid phase in the axial direction is used to calculate the storage utilization ratio of the EH-STES system, which relates the utilized thermal storage capacity to a theoretical thermal storage capacity. The storage utilization ratio is given by the maximum temperature difference between the HTF inlets $\Delta T_{in} = T_{f,in} - T'_{f,in}$:

$$\zeta = \frac{Q_{util.}}{Q_{th.}} = \frac{\int_0^{z^*=1} \left(T_{EH-STES}(t^* = \tau z^*) - T'_{EH-STES}(t^* = \tau' z^*)\right) dz^*}{T_{f,in} - T'_{f,in}} \tag{19}$$

In addition, this ratio is also given for the STES unit by:

$$\zeta_{TES} = \frac{Q_{TES,util.}}{Q_{TES,th.}} = \frac{\dot{m}_f\, \tau\, c_{p,f} \left(\overline{T}'_{f,STES,out} - T'_{f,in}\right)}{m_{TES}\, c_{p,TES} \left(T_{f,EFH,out} - T'_{f,in}\right)} \tag{20}$$

where m_{TES} is the storage mass with the appropriate heat capacity $c_{p,TES}$ and $T_{f,EFH,out}$, which is the TES charging temperature caused by the EFH component (see Fig. 2).

In the case of $\zeta_{TES} = 1$ or $\zeta = 1$ for $\Phi = 0$, the thermal reservoir is ideally utilized with a thermal front crossing the entire storage inventory during cyclic operation. As a consequence of the PtH implementation ($\Phi > 0$), utilization ratios larger than one are feasible, thus demonstrating the benefit of capacity enhancement.

3.4. Coefficient of uniformity

In contrast to the utilization ratio, the coefficient of uniformity is a performance-related KPI and describes the uniformity of the discharge temperature at the hot end of the storage tank. It can be expressed as the ratio of fluctuating thermal power to a uniform power output during discharging. Reducing the heat capacity rates, the ratio can be expressed by:

$$\xi = \frac{\dot{\overline{Q}}_{f,out}}{\dot{Q}_{f,out,max}} = \frac{\int_0^{t^*=1} \left(T'_f(t^*, z'^* = H) - T'_{f,in}\right) dt^*}{T_{f,in} - T'_{f,in}} \tag{21}$$

The coefficient of uniformity is also given for the STES by:

$$\xi_{TES} = \frac{\dot{\overline{Q}}_{f,TES,out}}{\dot{Q}_{f,TES,out,max}} = \frac{\overline{T}'_{f,STES,out} - T'_{f,in}}{T_{f,EFH,out} - T'_{f,in}} = \frac{\Delta \overline{T}'_{f,TES}}{\Delta T'_{f,TES,max}} \tag{22}$$

Thus, a maximum averaged outlet temperature $\overline{T}'_{f,STES,out}$ leads to $\xi_{TES} = 1$ and $\xi = 1$ for $\Phi = 0$. For a PtH operation with $\Phi > 0$, the coefficient of uniformity can be increased to $\xi > 1$ for the storage system, which would enable an advantageous bypass operation to ensure uniform power output at the mixing point.

Table 1
Material combinations for EFH and STES satisfying $\mathbf{f_{mat}} = 0.60$

Materials/property	$\overline{\rho}$ (kg m^{-3})	$\overline{c_p}$ (J kg^{-1} K^{-1})	$\overline{\rho c_p}$ (kJ m^{-3} K^{-1})
EFH-mat1: stainless steel	7700	448	344.96
STES-mat1: oxide ceramics	2300	900	2070.0
EFH-mat2: silicon carbide	3210	1060	344.96
STES-mat2: quartzite	2500	828	2070.0

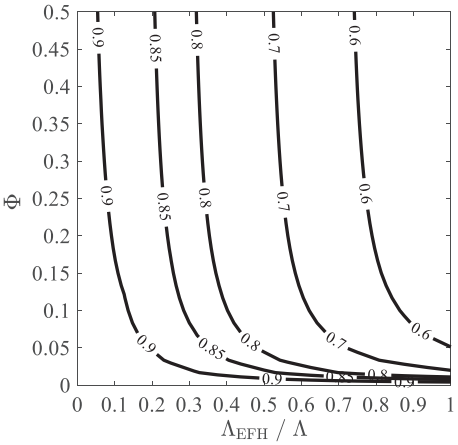

Fig. 3. Contour lines for thermodynamic efficiency $\eta_{EH-STES}$ of the storage system ($\Pi = 100$; $\Lambda = 100$).

4. Simulation setup

The Eq. (3a) through Eq. (4b) are implemented using the commercial simulation tool MATLAB R2019a. The temporal variable temperature profiles are obtained using the implicit centered method for Eqs. (3a) and (3b). The spatially discretized differential Eqs. (4a) and (4b) are solved numerically using the backward finite difference method. Therefore, the uniformly meshed EH-STES model is discretized in $N = 400$ compartments for the total reduced length Λ. In addition, the modeling approach for the STES component (Eqs. (3a) and (4a)) was confirmed using the one-dimensional continuous solid phase model from Ismail et al. [16]. Results for this comparison are presented in Appendix A.

Computations are started from an initial completely discharged state ($\overline{T_s} = 0$). After a transient cyclic mode with a fluid charging ($T_{f,in} = 1.0$ at Ω_L) and discharging ($T'_{f,in} = 0$ at Ω_R) inlet temperatures, the computation stops once the cyclic change of the delivered thermal energy falls below 10^{-4} J. This criterion is reached after six to eight cycles for design configurations with $\Pi = 100$ and $\Lambda = 100$. The corresponding computing time for each cycle additionally depends on the heat source number Φ and ranges from 4.5 to 5.4 s.

5. Results and discussion

In the following subsections, simulation studies based on the Φ-Λ-St model are conducted. First, the storage is investigated according to the location and extension of the EFH inside the storage tank. In the next step, the results for the introduced KPIs based on wide variations of Φ, Λ and Stanton numbers are discussed. This discussion reveals the improvements in storage performance and capacity due to the PtH extension.

5.1. Location and heat rate of the EFH

The analysis of the advantageous location and extension of the EFH is conducted by varying the dimensionless heat source number Φ and the heating area $z_{EFH} = \Lambda_{EFH}/\Lambda$ (see Fig. 2). This value increases from the

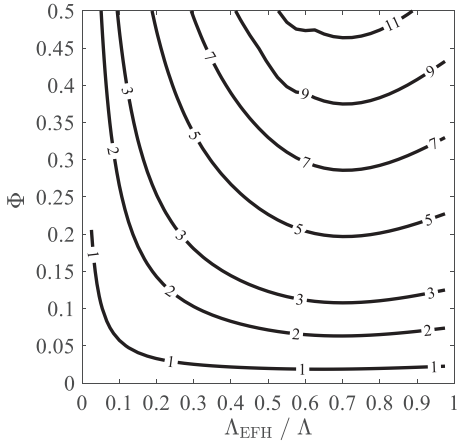

Fig. 4. Contour lines for gravimetric energy density $q_{EH-STES}$* in kJ/(kg K) of the EH-STES system (Π = 100; Λ = 100).

hot end ($z_{EFH} = 0$) of the thermal reservoir, reaching the cold end at $z_{EFH} = 1$. Moreover, the material related factor $f_{mat} = 0.60$ (see Eq. (9)) is applied for further investigations. Feasible material combinations for EFH and STES satisfying $f_{mat} = 0.60$ are presented in Table 1.

Fig. 3 presents the results for the thermodynamic efficiency of the EH-STES system for an example design configuration with a reduced regenerator length Λ = 100 and reduced period duration Π = 100. The contour lines for thermodynamic efficiency decrease with increased Λ_{EFH}/Λ ratio and heat source numbers Φ due to the growing exit loss at the cold end of the thermal reservoir. In contrast, small heating areas and small Φ cause high storage efficiencies but result in low gravimetric energy densities as indicated in Fig. 4. Nevertheless, there is a beneficial operation mode for small heating areas and high heat source numbers. For heating areas $z_{EFH} < 0.20$ and $\Phi \gg 0$, the heater outlet temperature significantly increases, resulting in high values for the energy density while still maintaining a high storage efficiency greater than 0.85. This effect is particularly pronounced for $\Phi > 0.20$ where the thermodynamic efficiency is only marginally affected by the increasing heat source. Qualitatively, the resulting contour lines remain similar for other values of Λ and Π. Thus, small heating masses heated with $\Phi \gg 0$ and located at the hot end of the EH-STES system are beneficial in terms of an energetic evaluation.

5.2. Impact on thermal storage capacity

For a compact presentation and a better interpretation of the following results, the parameter C_{TES} is introduced expressing the ratio of Λ to Π for the TES component. This relationship is valid for the cyclic operation and is given by Eq. (23), which extends the expression for Λ_{TES}/Π_{TES} by the TES inventory volume V_{TES}:

$$C_{TES} = \frac{\Lambda_{TES}}{\Pi_{TES}} = \frac{\rho_{TES}\, c_{p,TES}\, H\, (1-\varepsilon)\, V_{TES}}{w_f\, \rho_f\, c_{p,f}\, \tau\, \varepsilon\, V_{TES}} = \frac{m_{TES}\, c_{p,TES}}{\dot{m}_f\, c_{p,f}\, \tau} \tag{23}$$

This equation can be further extended by the temperature ratio $\Delta\overline{T}'_{f,TES}/\Delta T'_{f,TES,max}$ from Eq. (22). An additional substitution of Eq. (21) into Eq. (20) expresses C_{TES} by the ratio of ξ_{TES} to ζ_{TES}:

$$C_{TES} = \frac{m_{TES}\, c_{p,TES} * \Delta T'_{f,TES,max}}{\dot{m}_f\, c_{p,f}\, \tau * \Delta\overline{T}'_{f,TES}} * \frac{\Delta\overline{T}'_{f,TES}}{\Delta T'_{f,TES,max}} =$$

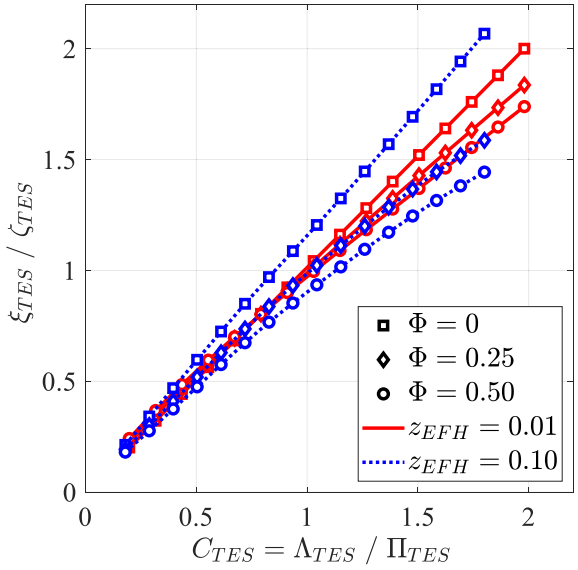

Fig. 5. Proportionality of ξ_{TES} to ζ_{TES} ratio and C_{TES} for Φ = [0 : 0.5], z_{EFH} = 0.10 and z_{EFH} = 0.01.

$$= \frac{Q_{TES,th.}}{\dot{Q}_{f,TES,out,max}\, \tau} = \frac{\xi_{TES}}{\zeta_{TES}} = \frac{\Lambda_{TES}}{\Pi_{TES}} \text{ for } \Phi = 0 \text{ and } z_{EFH} = 0 \tag{24}$$

The Λ_{TES} to Π_{TES} ratio given in Eq. (24) is the proportion of the theoretical thermal storage capacity $Q_{TES,th.}$ to the maximum thermal energy $Q_{f,TES,out,max.}$ delivered by the storage during discharging. Thus, C_{TES} is interpreted as the ratio of the storage size to the amount of energy delivered, which is inversely proportional to q_{TES}* according to Eq. (17a). Moreover, this interpretation could be used for investment decisions where the capital costs are set in relation to the revenues generated from energy sales.

The relationship from Eq. (24) is derived for Φ = 0 and $z_{EFH} = 0$; nonetheless, the preceding interpretation of C_{TES} could also be used for $\Phi > 0$ and $z_{EFH} > 0$ according to Fig. 5. Here, both the cases with and without PtH are compared for two heating areas. This comparison shows that with increasing heat source numbers and heating areas, the results

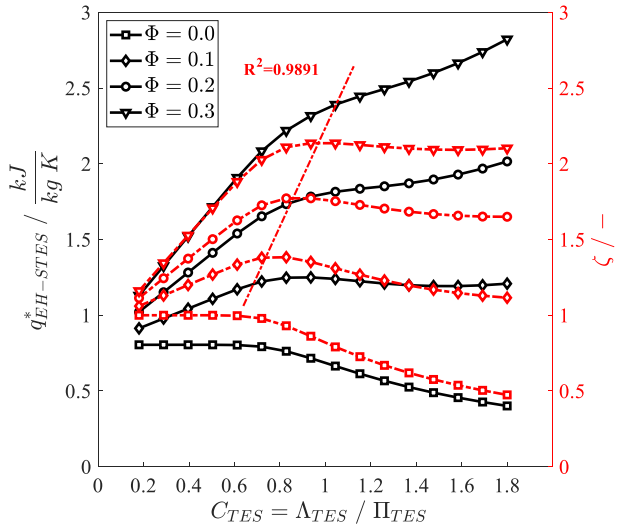

Fig. 6. Gravimetric energy density and storage utilization ration related to Λ and Φ for Π = 100 and $\Lambda_{EFH}/\Lambda = 0.10$

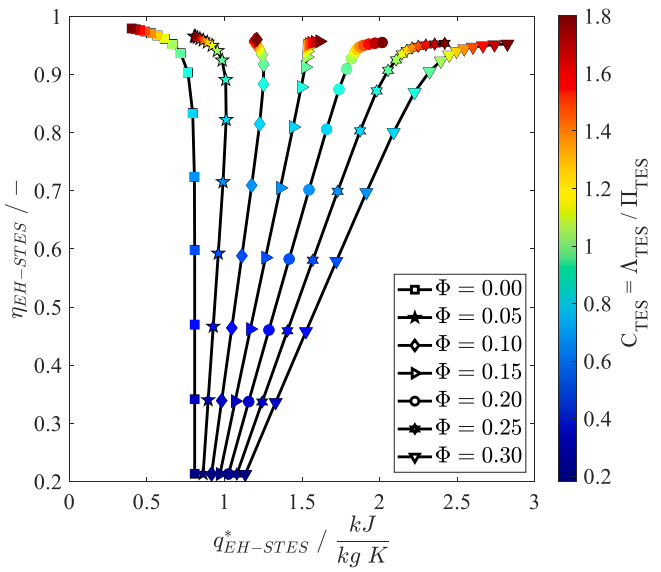

Fig. 7. Thermodynamic efficiency related to Λ and Φ for Π = 100 and Λ_{EFH}/Λ = 0.10

noticeably deviate from the bisector. Nevertheless, the proportionality remains for small heating areas ($z_{EFH} = 0.01$). Although for larger z_{EFH} in combination with $\Phi > 0$ this linearity is slightly damped, the behavior is still interpreted as proportional:

$$C_{TES} = \frac{\xi_{TES}}{\zeta_{TES}} \sim \frac{\Lambda_{TES}}{\Pi_{TES}} \text{ for } 0 < \phi < 0.5 \text{ and } 0 < z < 0.10 \tag{25}$$

Increasing the capacity of the storage tank through inner heat sources results in higher losses in efficiency (see Section 5.1). This effect primarily depends on the heat source number Φ, Λ and Π. To analyze the trade-off between these losses and the energy density, simulation studies varying the characteristic parameters Λ in range from 20 to 200 and Φ from 0 to 0.30 for Π = 50, 100 and 200 are performed. Moreover, the EH-STES system operates in cyclic mode with periodic charging and discharging cycles, in which a heating area $z_{EFH} = 0.10$ is chosen based on the findings from Section 5.1.

The results of the capacity-related KPI are discussed in relation to the PtH implementation before the performance-related results for the thermodynamic efficiency are presented. Fig. 6 depicts the gravimetric energy density and the storage utilization ratio in relation to the Λ_{TES} to Π_{TES} ratio and heat source number Φ. For the reference case without PtH (Φ = 0), there is a limitation of the gravimetric energy density, which is solely caused by material properties since the maximum solid media temperature is determined by the inlet temperature $T_{f,in}$. The inverse proportional relationship from Eq. (17a) explains the continuous decrease of gravimetric energy density for increasing C_{TES} (Fig. 7 shows again this relationship and additionally illustrates the effect on thermodynamic efficiency).

In contrast to the reference case, the gravimetric energy density increases for $\Phi > 0$ due to heating temperatures $T_{f,EFH,out} > 1.0$. This characteristic is attributable to the curve progression of the utilization ratio ζ (dashed lines in Fig. 6), which increases for $0.20 < C_{TES} < 0.80$ due to higher storage utilization in small and additionally heated reservoirs. The subsequent drop for $C_{TES} > 0.80$ results from the dominating increase of the thermal storage capacity provided by large reservoirs. The dashed regression line in Fig. 6 describes the positions of the maximum utilization ratios, which are given by:

$$\zeta_{max} = 3.25\ C_{TES} - 1.0 \ \forall\ C_{TES} \in [0.615,\ 1.12] \tag{26}$$

indicating a high coefficient of determination of $R^2 = 0.9891$. In addition, the maximum utilization ratio may be expressed as a linear function of the dimensionless heat source number $\zeta_{max} = 3.65\ \Phi + 1.0$ with $R^2 = 0.9984$ and $0 \le \Phi \le 0.50$. Combining Eqs. (23) and (26), the maximum utilization ratio may be either expressed with respect to the storage mass or the mass flow rate for given material properties and operating durations.

In addition to the capacity-related KPI presented in Fig. 6, Fig. 7 provides the findings for the thermodynamic efficiency for the previous discussion on beneficial Λ_{TES} to Π_{TES} ratios. These results illustrate that regardless of the energy density, small thermal reservoirs with $0.20 < C_{TES} < 0.80$ indicate low thermodynamic efficiency <85%. In contrast, a high efficiency >85% is achieved for large reservoirs with $C_{TES} > 0.80$ due to the decreasing exit loss at cold end of the thermal reservoir.

Furthermore, Fig. 7 illustrates the impact of PtH on the energy density for various heat source numbers. For $\Phi < 0.10$, the energy density significantly decreases with increases in the reservoir size ($C_{TES} > 0.80$). In contrast, the thermodynamic efficiency increases so that either a maximum energy density or efficiency can be achieved. This behavior has already been discussed in literature [14,22] for the reference case without external heat sources (Φ = 0). Integrating PtH with heat source numbers $\Phi > 0.10$ allows rising values for both the thermodynamic efficiency and energy density. Thus, large thermal reservoirs with short charging and discharging periods ($C_{TES} > 1$) not only lead to high efficiency but also to high energy density, whereby higher heat source numbers result in a slight loss in efficiency. This loss is marginal comparing constant C_{TES} values; however, the energy density significantly increases with higher heat source numbers: a heat source number of Φ = 0.30 results in an efficiency drop of 3.3 percentage points for $C_{TES} = 1.0$ but increases the gravimetric energy density from 0.66 kJ/kg K at Φ = 0 to 2.39 kJ/kg K.

Demanding a high energy density in addition to high efficiency leads to EH-STES design configurations that suggest either $C_{TES} > 1.0$ for $\Phi > 0.10$ or $0.80 < C_{TES} \le 1.0$ for $\Phi \le 0.10$. Here, a heat source number of Φ = 0.10 leads to a loss in thermodynamic efficiency by a maximum of 2.0 percentage points but an improvement in gravimetric energy density by 63.7% for $C_{TES} = 0.80$ and 86.7% for $C_{TES} = 1.0$.

Additional results from simulation studies for Π = 50 and Π = 200 show analogous curve characteristics compared to those presented in Figs. 6 and 7; however, the maximum value for the utilization ratio shifts to $C_{TES} = 0.75$ for Π = 50 and $C_{TES} = 1.05$ for Π = 200. In conclusion, the EH-STES designs that provide maximum thermal utilization for a given Φ as well as a thermodynamic efficiency greater than 90% are identified for Λ_{TES} to Π_{TES} ratios in the range of 0.75 to 1.05 for Π = [50:200].

5.3. Impact on storage performance

A major requirement for the process integration of STES units is the constant power output during discharging. Since counterflow regenerator storage experiences an inevitable drop in discharge power, many authors propose a bypass operation to sustain the outlet temperature at the mixing point for the entire discharging period [15,20]. In this case, the coefficient of uniformity is limited to ξ = 1, which leads to the mixing temperature $T'_{f,out,mix} < T_{f,in}$ due to irreversible losses during the cyclic operation. Conversely, integrating PtH with $\Phi > 0$ results in higher storage temperature that hypothetically leads to higher outlet and mixing temperature $T'_{f,out,mix} > T_{f,in}$ compared to the case without an EFH. Therefore, further investigation focuses on the effects of the PtH integration on the discharging performance by evaluating the coefficient of uniformity and the achieved averaged outlet temperature $\overline{T}'_{f,out}$. For this purpose, simulation studies are performed with target values for the outlet temperature drop at a given thermodynamic efficiency of 90%. The permissible outlet temperature drop $\Delta T_{f,drop}$ at the end of the discharging period is specified with 10%, 20% and 30% related to the inlet temperature $T_{f,in} = 1$. The additional specification of the thermodynamic efficiency is needed to limit the heat source number Φ (otherwise, arbitrarily high coefficients of uniformity might be achieved). Thus, the

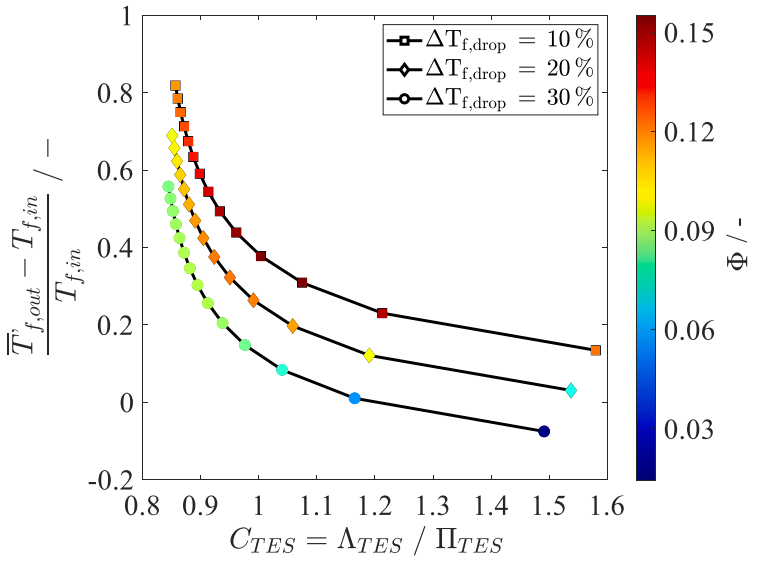

Fig. 8. Nominal temperature raise of the averaged outlet temperature $T'_{f,out}$ during discharging for $\eta_{EH\text{-}STES} = 90\%$, $\Delta T'_{f,drop} = 10\text{–}30\%$ and $\Lambda_{EFH}/\Lambda = 0.10$

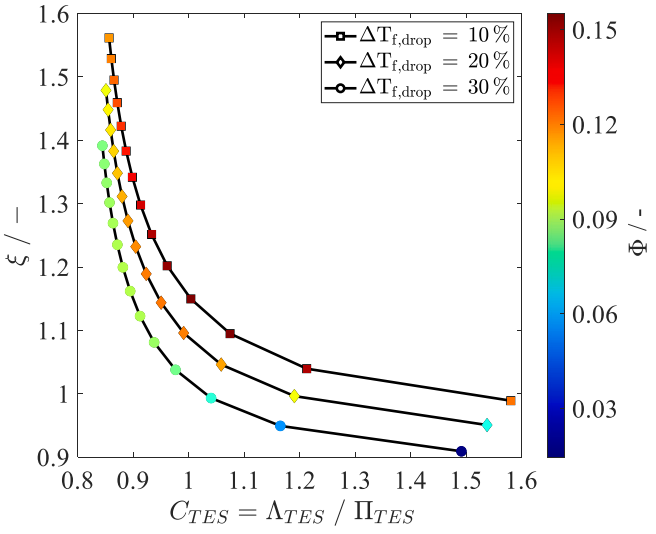

Fig. 9. Coefficient of uniformity as a function of C_{TES} and Φ for $\eta_{EH\text{-}STES} = 90\%$, $\Delta T'_{f,drop} = 10\text{–}30\%$ and $\Lambda_{EFH}/\Lambda = 0.10$.

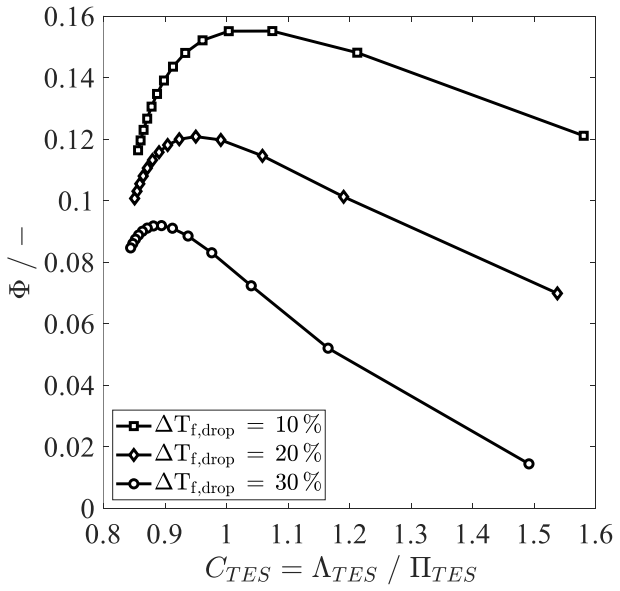

Fig. 10. Dimensionless heat source number as a function of C_{TES} for $\eta_{EH\text{-}STES} = 90\%$, $\Delta T'_{f,drop} = 10\text{–}30\%$ and $\Lambda_{EFH}/\Lambda = 0.10$

parameters Λ and Φ are iteratively calculated varying Π = [20:150] for the given temperature drop and thermodynamic efficiency at a heating area $\Lambda_{EFH}/\Lambda = 0.10$.

The results presented in Figs. 8 and 9 illustrate the increased performance and flexibility through the PtH integration. A significantly higher power output caused by the higher averaged temperature $\overline{T}'_{f,out}$ (Fig. 8) is achieved. In addition, values for the coefficient of uniformity with $\xi > 1$ (Fig. 9) are obtained, indicating the potential for a beneficial bypass operation. Design solutions ranging in $0.85 < C_{TES} < 1.60$ for $0 < \Phi \leq 0.15$ are feasible to ensure 90% efficiency at the given temperature drop. Considering Eq. (23), this flexibility could be used for cost savings by decreasing components' size due to the increased gravimetric energy density.

Furthermore, Fig. 9 shows that high heat source numbers are either achieved for small temperature drops and a constant reservoir size or for small reservoir sizes and a constant outlet temperature drop. Since short thermal reservoirs generally suffer from a high outlet temperature drop, the EFH compensates with a high heat source number to achieve the targeted value, for instance $\Delta T_{f,drop} = 20\%$. Moreover, this compensation effect increases as the permissible temperature drop decreases, resulting in a high heat source number. Fig. 10 additionally illustrates that the heating source does not continuously rise with falling C_{TES} values. The curve profiles indicate two feasible STES design configurations with the same heat source number for any given temperature drop: one configuration with a small Λ_{TES} to Π_{TES} ratio < 1.0 and another with a high ratio > 1.0. According to Eq. (11), small reservoirs with a small heating volume V_{EFH} are heated by a high Joule heat power to compensate for the less efficient heat transfer due to the small surface area to volume ratio a_v and vice versa.

Altogether, the PtH integration increases the storage performance and flexibility since a higher power output together with a higher coefficient of uniformity is achieved without decreasing the thermodynamic efficiency. Moreover, high heat source numbers up to Φ = 0.15 allow for compact EH-STES design configurations ($0.85 < C_{TES} < 1.0$) with a high output power and thermodynamic efficiency at 90%.

6. Conclusions

A transient thermodynamic model is developed for the electrically heated solid media based thermal energy storage (EH-STES) to identify high performing and energy-efficient design solutions with a high thermal storage capacity. The compact and dimensionless modeling approach enables the characterization of such a hybrid storage system by introducing characteristic parameters such as the dimensionless heat source number Φ, the dimensionless storage length Λ and the period duration Π. Based on these parameters, the key performance indicators (KPIs) of energy density, storage utilization ratio, coefficient of uniformity and thermodynamic efficiency are derived to evaluate the improvement in thermal storage capacity and performance due to the power-to-heat integration.

Simulation studies varying the characteristic parameters are conducted to identify general design solutions with high values for the defined KPIs. The results for thermodynamic efficiency and energy density indicate that integrating a small and powerful electrical fluid heater at the hot end of the thermal reservoir is beneficial in terms of energetic and exergetic efficiency. In contrast to an operation without a power-to-heat extension ($\Phi = 0$) where either a high efficiency or a high energy density is achieved, the operation with heat source numbers $\Phi > 0.10$ in large thermal reservoirs ($\Lambda_{TES}/\Pi_{TES} > 1.0$) allows for the first time high values for both the efficiency and energy density. The comparison with the reference case ($\Phi = 0$) reveals an increase of 60% for the energy density at efficiencies above 0.90. These results are obtained together with maximum storage utilization ratios ($\zeta_{max} = 3.65\,\Phi + 1.0$), which convey a significant improvement in thermal storage capacity for $\Phi > 0$.

Another major conclusion related to generalized storage design is that EH-STES design configurations close to $\Lambda_{TES}/\Pi_{TES} \cong 1.0$ and heated with heat source numbers $\Phi < 0.15$ result in a high thermal storage capacity along with a high discharging performance at efficiencies above 0.90. To meet demands for a higher thermal storage capacity, the heat source number could be increased to $\Phi \gg 0.15$, albeit with increasing efficiency losses.

CRediT authorship contribution statement

Sergej Belik: Conceptualization, Methodology, Software, Data curation, Investigation, Writing-Original draft, Visualization. **Volker Dreissigacker**: Investigation, Writing- Reviewing and Editing. **Stefan Zunft**: Writing-Reviewing and Editing, Supervision.

Declaration of competing interest

The authors declare that they have no known competing financial interests or personal relationships that could have appeared to influence the work reported in this paper.

Appendix A

Fig. A1 shows the comparison between the calculated temperature profiles from the dimensionless modeling approach presented in chapter 2 (Eqs. (3a) and (4a)) and the continuous solid phase model introduced by Ismail et al. [16] for the STES unit. Both models are discretized in four hundred compartments for the reduced regenerator length $\Lambda = 100$ ($\Lambda_{EFH} = 0$). For the detailed model from [16], a storage tank with a length and diameter of 10 m each is chosen. In addition, the STES-mat1 material from Table 1 with a thermal conductivity of 3.0 W m^{-1} K^{-1}, a void fraction of 40% and a particle diameter of 44.25 mm is assumed for the packed bed. Furthermore, the charging and discharging period is varied from 3.37 h to 6.0 h to modify Π and thus C_{TES} from 1.60 to 0.90. The results for the fluid temperature show a good agreement with the detailed model from [16]. The largest deviation of up to 5% occurs for $C_{TES} = 1.60$ due to the greater influence of heat conduction in large storage tanks, which is neglected in the proposed model.

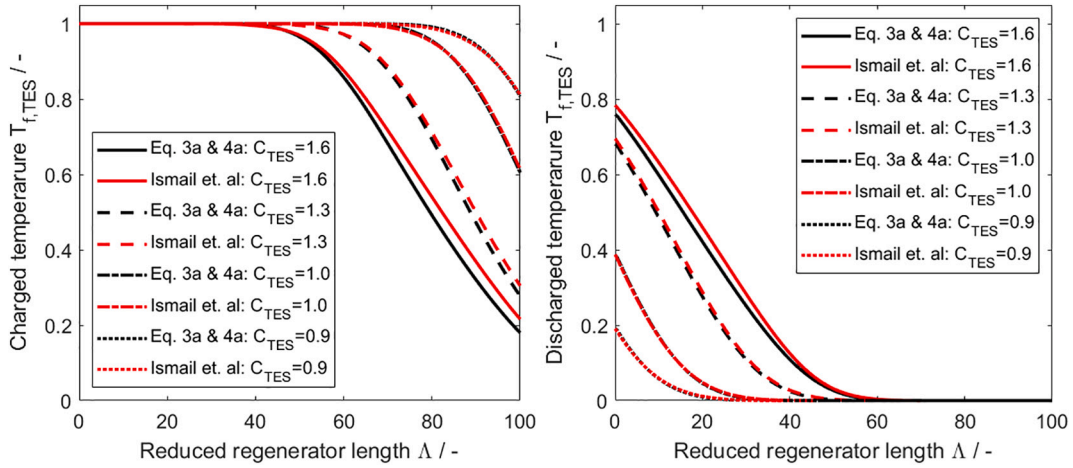

Fig. A1. Normalized fluid temperature profiles under cyclic operation at the last time step of respective charging and discharging for $\Lambda = 100$ and different C_{TES} used in the study from chapter 5 ($\Gamma_{TES} = 0$ and $\Lambda_{EFH} = 0$).

References

[1] Franz Trieb, André Thess, Storage plants–a solution to the residual load challenge of the power sector? J. Energy Storage 31 (2020) https://doi.org/10.1016/j.est.2020.101626.

[2] C.-P. Bartsch, tructural change and plant repurposing in the Rhenish lignite mining area, RWE, Presentation given at 6th working group meeting of "Platform for coal regions in transition". https://ec.europa.eu/energy/sites/ener/files/documents/5.3._master_coal_plant_repurposing.pdf, 2021. (Accessed 16 April 2021).

[3] MAN, Energy Storage. "Electro-thermal energy storage". https://www.man-es.com/energy-storage/solutions/energy-storage/electro-thermal-energy-storage, 2021. (Accessed 16 April 2021).

[4] Alberto Benato, Anna Stoppato, Energy and cost analysis of a new packed bed pumped thermal electricity storage unit, J. Energy Resour. Technol. 140 (2) (2018), https://doi.org/10.1115/1.4038197.

[5] Daniel C. Stack, Daniel Curtis, Charles Forsberg, Performance of firebrick resistance-heated energy storage for industrial heat applications and round-trip electricity storage, Appl. Energy 242 (2019) 782–796, https://doi.org/10.1016/j.apenergy.2019.03.100.
[6] Philipp Vinnemeier, et al., Integration of heat pumps into thermal plants for creation of large-scale electricity storage capacities, Appl. Energy 184 (2016) 506–522, https://doi.org/10.1016/j.apenergy.2016.10.045.
[7] Charles W. Forsberg, et al., Converting excess low-price electricity into high-temperature stored heat for industry and high-value electricity production, Electr. J. 30 (6) (2017) 42–52, https://doi.org/10.1016/j.tej.2017.06.009.
[8] Schniewindt, Flow Heaters, 2021. https://www.schniewindt.de/en/csn-flow-heaters/. (Accessed 15 April 2021).
[9] Ohmex, Electrical Process Flow Heaters datasheet, in: https://www.ohmex.de/en/wp-content/uploads/sites/3/2020/03/electric-process-heater_STR_2020-03.pdf, 2021. (Accessed 15 April 2021).
[10] Kanthal®, Resistance heating alloys and systems for industrial furnaces. https://www.kanthal.com/globalassets/kanthal-global/downloads/materials-in-wire-and-strip-form/resistance-heating-wire-and-strip/home-appliance_s-ka026-b-eng_lr.pdf, 2021. (Accessed 1 May 2021).
[11] Markus Hänchen, Sarah Brückner, Aldo Steinfeld, High-temperature thermal storage using a packed bed of rocks–heat transfer analysis and experimental validation, Appl. Therm. Eng. 31 (10) (2011) 1798–1806, https://doi.org/10.1016/j.applthermaleng.2010.10.034.
[12] H. Hausen, Wärmeübertragung im Gegenstrom, Gleichstrom und Kreuzstrom, Springer, Berlin, Heidelberg, 1976.
[13] T.E.W. Schumann, Heat transfer: a liquid flowing through a porous prism, J. Frankl. Inst. 208 (1929) 405–416.
[14] F.W. Schmidt, A.J. Willmott, Thermal Energy Storage and Regeneration, Hemisphere Press, 1981.
[15] Ryan Anderson, et al., Packed bed thermal energy storage: a simplified experimentally validated model, J. Energy Storage 4 (2015) 14–23, https://doi.org/10.1016/j.est.2015.08.007.
[16] K.A.R. Ismail, R. Stuginsky Jr., A parametric study on possible fixed bed models for pcm and sensible heat storage, Appl. Therm. Eng. 19 (7) (1999) 757–788, https://doi.org/10.1016/S1359-4311(98)00081-7.
[17] Anton Meier, Christian Winkler, Daniel Wuillemin, Experiment for modelling high temperature rock bed storage, Solar Energy Mater. 24 (1-4) (1991) 255–264, https://doi.org/10.1016/0165-1633(91)90066-T.
[18] Ryan Anderson, et al., Experimental results and modeling of energy storage and recovery in a packed bed of alumina particles, Appl. Energy 119 (2014) 521–529, https://doi.org/10.1016/j.apenergy.2014.01.030.
[19] Harmeet Singh, R.P. Saini, J.S. Saini, A review on packed bed solar energy storage systems, Renew. Sustain. Energy Rev. 14 (3) (2010) 1059–1069, https://doi.org/10.1016/j.rser.2009.10.022.
[20] Thibaut Esence, et al., A review on experience feedback and numerical modeling of packed-bed thermal energy storage systems, Solar Energy 153 (2017) 628–654, https://doi.org/10.1016/j.solener.2017.03.032.
[21] Syed M. Zubair, Meamer El-Nakla, Shahzada Z. Shuja, Thermoeconomic design and analysis of a sensible-heat thermal energy storage system with Joulean heating of the storage element, Exergy Int. J. 2 (4) (2002) 237–247, https://doi.org/10.1016/S1164-0235(02)00074-2.
[22] Volker Dreißigacker, Sergej Belik, System configurations and operational concepts for highly efficient utilization of power-to-heat in A-CAES, Appl. Sci. 9 (7) (2019) 1317, https://doi.org/10.3390/app9071317.
[23] Sammy Houssainy, et al., Thermodynamic analysis of a high temperature hybrid compressed air energy storage (HTH-CAES) system, Renew. Energy 115 (2018) 1043–1054, https://doi.org/10.1016/j.renene.2017.09.038.